JOURNAL OF GEOPHYSICAL RESEARCH, VOL. 107, NO. A8, 1214, 10.1029/2001JA000217, 2002

# Effects of large horizontal winds on the equatorial electrojet

D. L. Hysell[1]
Department of Physics and Astronomy, Clemson University, Clemson, South Carolina, USA

J. L. Chau
Radio Observatorio de Jicamarca, Instituto Geofísico del Perú, Lima, Peru

C. G. Fesen
W. B. Hanson Center for Space Sciences, University of Texas at Dallas, Richardson, Texas, USA

Received 20 July 2001; revised 28 September 2001; accepted 14 November 2001; published 28 August 2002.

[1] The effects of large winds on the low-latitude *E* region ionosphere and the equatorial electrojet in particular are analyzed theoretically, computationally, and experimentally. The principles that govern the relationship between electric fields, currents, and winds in steady flows in the ionosphere are reviewed formally. A three-dimensional numerical model of low-latitude ionospheric electrostatic potential is then described. Scaled wind profiles generated by the National Center for Atmospheric Research (NCAR) thermosphere/ionosphere/mesosphere electrodynamics general circulation model (TIME-GCM) are used as inputs for the potential model. The model shows that the horizontal wind component drastically modifies the vertical polarization electric field in the electrojet and drives strong zonal and meridional currents at higher dip latitudes outside the electrojet region. Comparison between the model output and coherent scatter radar observations of plasma irregularities in the electrojet indicate that strong winds and wind shears are present in the *E* region over Jicamarca that are roughly consistent with NCAR model wind predictions if the amplitudes of the latter are increased by about 50%. *INDEX TERMS:* 2411 Ionosphere: Electric fields (2712); 2415 Ionosphere: Equatorial ionosphere; 2427 Ionosphere: Ionosphere/atmosphere interactions (0335); 2439 Ionosphere: Ionospheric irregularities; *KEYWORDS:* equatorial electrojet, ionospheric currents, neutral winds

## 1. Introduction

[2] In this paper, we examine the effects of large horizontal neutral winds on the equatorial electrojet and low-latitude ionospheric current system. While it has long been suspected that very large winds and wind shears are present in the electrojet [*Kudeki et al.*, 1987], only recently have such winds been observed directly [*Larsen and Odom*, 1997], and only recently are comparable winds beginning to be predicted by global circulation models such as the NCAR thermosphere/ionosphere/mesosphere electrodynamics general circulation model (TIME-GCM) [*Roble and Ridley*, 1994; *Roble*, 1995]. The cause and structure of large winds in the lower thermosphere were foci of the Clemson 2000 conference, to be reported on in an upcoming issue of *Journal of Atmospheric and Solar-Terrestrial Physics*. Here, we evaluate the effects of the winds on *E* region ionospheric electrodynamics and on the electrojet in particular.

[3] The interaction between the lower thermospheric winds and the ionospheric plasma is qualitatively different at the dip equator compared to other latitudes. Winds are most prone to generate dynamo electric fields where the magnetic field lines are nearly horizontal, and the Cowling conductivity in the equatorial *E* region provides a mechanism for the amplification of the dynamo fields. The effects of winds on electrojet electrodynamics have been studied theoretically by *Richmond* [1973], *Kato* [1973], *Fambitakoye et al.* [1976], *Forbes and Lindzen* [1976], *Anandarao et al.* [1977], *Anandarao and Raghavarao* [1979], and *Reddy and Devasia* [1978] among others. Many of their results were summarized by *Forbes* [1981] and will be referred to throughout this text. It has been shown that horizontal winds can drastically affect electric fields and currents locally in the electrojet, although the effects may be difficult to detect with ground-based magnetometers due to destructive interference. Observing the effects of winds in the electrojet with radar remote sensing is complicated by the almost constant presence of ionospheric irregularities. These irregularities render conventional incoherent scatter radar techniques unusable.

[4] A number of investigators have attempted to estimate ionospheric electric fields and winds indirectly from coherent radar backscatter from plasma irregularities in the electrojet [*Balsley*, 1973; *Balsley et al.*, 1976; *Reddy and Devasia*, 1981; *Reddy et al.*, 1987; *Devasia and Reddy*, 1995; *Hysell and Burcham*, 2000; *Chau et al.*, 2000]. The various experimental techniques employed differ in their

[1]Now at Earth and Atmospheric Sciences, Cornell University, Ithaca, New York, USA.


0148-0227/02/2001JA000217$09.00

details but all make use of the fact that the phase speeds of plasma waves in the electrojet are thought to be known functions of the electric field, temperature, and neutral wind velocity. In practice, deriving reliable neutral wind speed estimates from coherent scatter radar measurements is difficult because the functional dependence of the data on the neutral wind velocity is not unique. Statistical fluctuations in the radar data make the data inversion process less reliable.

[5] In this paper, we solve the direct problem of predicting coherent scatter radar observations on the basis of an assumed neutral state rather than the more difficult inverse problem alluded to immediately above. We will use lower thermospheric neutral wind profiles predicted by the NCAR TIME-GCM as inputs to a static model of the low-latitude *E* region ionospheric potential. This latter model in turn will be used to predict the electric field perturbations that arise from the neutral wind forcing. The predictions will be compared with coherent scatter radar observations of plasma irregularities propagating in the equatorial electrojet. The model-data comparisons at once illustrate the effects that large winds can have on *E* region ionospheric electrodynamics and demonstrate that the effects are manifest in the equatorial ionosphere.

## 2. Model Fundamentals

[6] In this section, we describe formally the relationship between neutral winds, currents, and low-frequency electric fields in an ionospheric plasma. (Readers familiar with this topic may wish to skip ahead to section 3 where a numerical model of the electrojet is described.) The ionospheric current density **J** due to the Lorentz force on the plasma can be expressed as

$$\mathbf{J} = \sigma_P(\mathbf{E}_\perp + \mathbf{u}\times\mathbf{B}) + \sigma_H\hat{b}\times(\mathbf{E}_\perp + \mathbf{u}\times\mathbf{B}) + \sigma_\circ\mathbf{E}_\parallel \quad (1)$$

where **E** and **B** are the electrostatic field and magnetic induction, respectively, **u** is the neutral wind velocity, $\hat{b}$ is a unit vector parallel to the geomagnetic field, and where the $\perp$ and $\parallel$ subscripts denote directions perpendicular and parallel respectively to $\hat{b}$. Here, $\sigma_P$, $\sigma_H$, and $\sigma_\circ$ are the Pedersen, Hall, and parallel or direct conductivities:

$$\sigma_P = e^2\sum_j \frac{n_j\nu_j}{m_j(\nu_j^2+\Omega_j^2)} \quad (2)$$

$$\sigma_H = e^2\sum_j \frac{-n_j\Omega_j}{m_j(\nu_j^2+\Omega_j^2)} \quad (3)$$

$$\sigma_\circ = e^2\sum_j \frac{n_j}{m_j\nu_j} \quad (4)$$

where the sums are over electrons and ion species, *e* is the electron charge, $n_j$ is the number density, $\Omega_j$ is the gyrofrequency which carries the sign of the charge of species *j*, and $\nu_j$ is the collision frequency. Note that the Hall conductivity has been defined here and used throughout the paper in such a way that it is a positive quantity. Equation (1) can be interpreted as the current density in a frame of reference moving with the neutral wind velocity, with **E** representing the electric field in a stationary frame and $\mathbf{u}\times\mathbf{B}$ representing a coordinate transformation. However, current density in a plasma is invariant under Galilean transformation, and (1) therefore applies equally well in the stationary reference frame.

[7] Quasineutrality in the plasma imposes the constraint that the current density be solenoidal. In order to analyze the consequences of this constraint, we can decompose the electric field into a uniform, background component $\mathbf{E}_\circ$ and a perturbed, spatially-varying component $-\nabla\Phi$, where $\Phi$ is the electrostatic potential. The background component could represent a field imposed from outside the immediate region of interest such as the dawn-to-dusk zonal electric field present in the equatorial ionosphere, for example. To the extent that the currents driven by the wind and the background electric field are divergent, the perturbation electric field will emerge to preserve quasineutrality. These polarization electric fields arise from electric dipole moments induced in the plasma by the wind and the background electric field.

[8] Equating the divergence of the current density in (1) with zero shows that

$$\begin{aligned}\nabla'^2\Phi = {} & \nabla_\perp\ln\sigma_P\cdot(\mathbf{E}_\circ - \nabla_\perp\Phi + \mathbf{u}\times\mathbf{B}) + (\nabla\times\mathbf{u})\cdot\mathbf{B} \\ & + \frac{\sigma_H}{\sigma_P}\left[\nabla_\perp\ln\sigma_H\cdot\left(\hat{b}\times(\mathbf{E}_\circ - \nabla_\perp\Phi) + \mathbf{u}_\perp B\right) + (\nabla_\perp\cdot\mathbf{u})B\right] \\ & - \nabla'_\parallel\ln\sigma_\circ\cdot\nabla'_\parallel\Phi \end{aligned} \quad (5)$$

Here, we make use of the coordinate transformations $\nabla'_\parallel \equiv \sqrt{\sigma_\circ/\sigma_P}\nabla_\parallel$, $\nabla'^2_\parallel \equiv (\sigma_\circ/\sigma_P)\,\nabla^2_\parallel$, and $\nabla'^2 \equiv \nabla^2_\perp + \nabla'^2_\parallel$ introduced by *Farley* [1959, 1960] who studied the efficiency of transmission of transverse electric fields over long distances along magnetic field lines. Potential structures in the ionosphere are inherently isotropic due to the large ratio of parallel to Pedersen conductivities. This coordinate transformation is to a space elongated in the parallel direction in which potential structures are essentially isotropic. Written this way, (5) has the form of Poisson's equation, and all the terms on the right side of (5) can consequently be associated with polarization charge density. Sources of polarization charge density include neutral wind fields that are either divergent or rotational in the plane perpendicular to the magnetic field and winds flowing parallel or perpendicular to transverse gradients in the plasma conductivities. Polarization charge density indicates divergence in the plasma polarization, and that part of it identified with transverse divergence implies vorticity in $\mathbf{E}\times\mathbf{B}$ drifts. Such vorticity is clearly evident in high-latitude *E* region convection as well as in the evening vortex in the postsunset equatorial *F* region [*Haerendel et al.*, 1992; *Kudeki and Bhattacharyya*, 1999] and in strong shears in the equatorial electrojet electron drift velocities [*Kudeki et al.*, 1981].

[9] The solution for $\Phi$ in a region is specified by (5) and by the boundary conditions. If the winds are incompressible and invariant along the magnetic lines of force and if the boundary conditions permit it, (5) is solved for polarization electric fields arising transverse to **u** and $\hat{b}$ such that the total $\mathbf{E}\times\mathbf{B}$ drifts precisely match **u**. Little or no wind-driven current flows in that case since the electrons and ions move together with the neutrals. The right side of (5) is nonzero if **u** is rotational in the plane perpendicular to **B**. This phenom-

enon is the basis for dynamo theory [*Rishbeth*, 1971]. More developed forms of dynamo theory successfully predict many aspects of plasma circulation in the equatorial zone including super rotation and the prereversal enhancement [*Heelis et al.*, 1974; *Rishbeth*, 1981; *Fejer*, 1981; *Wharton et al.*, 1984; *Farley et al.*, 1986; *Haerendel and Eccles*, 1992; *Crain et al.*, 1993; *Du and Stening*, 1999].

[10] Conversely, if the winds vary along magnetic field lines, solutions to (5) necessitate potential variations in the direction of the magnetic field. Perpendicular polarization electric fields may not be required for (5) to be satisfied in this case, in which field-aligned currents flow and effectively "short out" the dynamo electric field in part or in whole. The wind drives current transverse to **B**, the current dissipates power by Joule heating and through mechanical work, and the associated ion drag contributes to the neutral wind momentum balance [*Larsen and Walterscheid*, 1995]. However, the transverse current is closed by the field-aligned currents, and the entire current remains solenoidal. If the winds are not stationary along the magnetic field lines, the wind-driven dynamo will not operate efficiently.

[11] Equation (5) shows that meridional winds are apt to have less influence on ionospheric electrodynamics than zonal winds for the following reasons. Field-aligned winds do not drive current in this model, and meridional winds should therefore have little electrodynamic effect near the dip equator except perhaps where the magnetic declination is large. Elsewhere, $\mathbf{u} \times \mathbf{B}$ currents associated with meridional winds are zonal and do not flow in the direction of strong conductivity gradients except immediately in the vicinity of the solar terminator. The $\mathbf{u}_\perp$ term in (5) receives only a small contribution from meridional winds except at relatively high dip latitudes where, once again, the induced current does not tend to flow in the direction of strong conductivity gradients. In any event, meridional winds are mainly ineffective in generating polarization electric fields since the wind forcing would tend to vary greatly along the magnetic field lines.

[12] Approximate but illustrative solutions to (5) can be obtained by treating magnetic field lines as equipotentials. This treatment is justified to some degree by the elongation of potential structures in the ionosphere in the direction of the geomagnetic field resulting from the large ratio of the parallel to Pedersen conductivities. The elongation factor $\sqrt{\sigma_\circ/\sigma_P}$ is of order $10^3$ in the *F* region where the magnetic field lines are well approximated as equipotentials in equilibrium. That factor falls to order 10 in the lower *E* region and to order unity in the *D* region, however, where the equipotential approximation begins to break down and approximations based on it fail.

[13] An equipotential ionospheric model was described by *Richmond* [1973] who assumed a dipole model for the geomagnetic field and considered an individual flux tube. Application of the divergence theorem to the quasineutrality condition indicates that the total current flux through the surface of the flux tube is identically zero. Assume further that there is no flux out the ends of the tube which extend below the ionosphere although field-aligned currents may exist within the volume of the tube. Figure 1 shows a representation of the magnetic flux tube in question. Let ($r$, $\theta$, $\phi$) represent polar coordinates and ($\alpha$, $\beta$, $\phi$) be components of an orthogonal magnetic coordinate system.

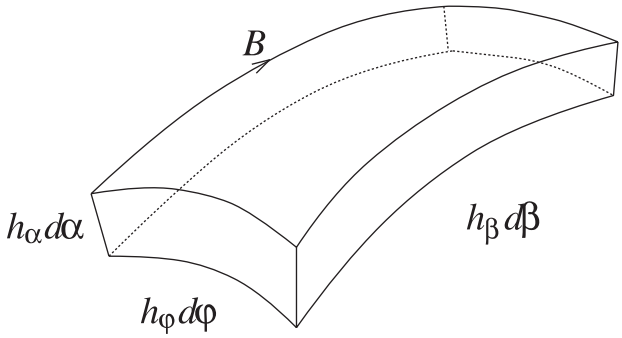


**Figure 1.** Schematic diagram of a magnetic flux tube. Terms like $h_\eta d\eta$ are orthogonal, differential arc length elements associated with the magnetic coordinates $\alpha$, $\beta$, and $\phi$ (see text).

Dipole magnetic field lines are traced by constant $\alpha$ curves of the form $r = \alpha \sin^2\theta$. Constant $\beta$ curves of the form $r^2 = \cos\theta/\beta$ are everywhere normal to the dipole field lines. The scale factors $h_\alpha$, $h_\beta$, and $h_\phi$ formally define a Euclidean metric for the magnetic coordinate system such that $ds^2 = h_\alpha^2\, d\alpha^2 + h_\beta^2 d\beta^2 + h_\phi^2 d\phi^2$, where $ds$ is a length element.

[14] The flux tube shown in Figure 1 is bounded by $\alpha$ = constant, $\beta$ = constant, and $\phi$ = constant surfaces. Consider the tube to be very thin vertically so that all of the flux through it passes through the $\alpha$ = constant surfaces. In the limit that the upper and lower $\alpha$ = constant surfaces become coincident, the quasineutrality condition then becomes

$$d\phi \int J_\alpha h_\phi h_\beta d\beta = \text{constant} \tag{6}$$

where $J_\alpha$ is the component of the current density normal to the $\alpha$ = constant surface of the flux tube and where the integration is along a magnetic field line. The constant here is the differential vertical *E* region current *dI* flowing in the interval $d\phi$ at the base of the flux tube. Since $J_\alpha$ vanishes at the lower boundary of the ionosphere, one can argue that this constant should be zero for a flux tube passing below the lower boundary and, consequently, for all the flux tubes above it. However net vertical current fluxes do arise in the electrojet, so this is only an approximation consistent with the stated assumptions.

[15] Since magnetic field lines are regarded as equipotentials, we may write $E_\phi h_\phi$ = constant and $E_\alpha h_\alpha$ = constant at all points on a given flux tube. Furthermore, the definitions in (1) make it clear that

$$J_\alpha = \sigma_P(E_\alpha + u_\phi B) - \sigma_H(E_\phi - u_\alpha B) \qquad \text{or}$$
$$J_\alpha h_\phi h_\beta = \sigma_P E_\alpha h_\phi h_\beta + \sigma_P u_\beta B h_\beta h_\beta - \sigma_H E_\phi h_\phi h_\beta + \sigma_H u_\alpha B h_\phi h_\beta$$

This last expression can then be substituted into the quasineutrality condition (6). Making use of the equipotential approximation, it is then possible to solve for either transverse electric field component in terms of the other and in terms of the neutral wind field. Assuming that the zonal electric field is known, the vertical electric field becomes:

$$E_\alpha = \frac{E_\phi h_\phi \int \sigma_H h_\beta d\beta - \int \left(\sigma_P u_\phi + \sigma_H u_\alpha\right) B h_\phi h_\beta d\beta + dI/d\phi}{h_\alpha \int \sigma_P \frac{h_\phi h_\beta}{h_\alpha} d\beta} \tag{7}$$

Equation (7) can be readily interpreted when applied to the equatorial zone where the three scale factors are nearly constants. The first term in the numerator of (7) shows how zonal electric fields in the equatorial $E$ region give rise to the strong vertical polarization electric fields that drive the electrojet. The second term in the numerator relates to polarization electric fields driven by the neutral wind dynamo. If $u_\phi$ is invariant along magnetic field lines, (7) predicts that polarization electric fields will arise such that the plasma $\mathbf{E} \times \mathbf{B}$ drifts match the neutral wind velocity. In this case, the dynamo process is efficient, and little wind-driven current flows. If, however, $u_\phi$ varies along the magnetic field line, the polarization electric field that arises will represent a Pedersen-conductivity-weighted average of the neutral wind forcing. If the neutral wind oscillates along the path of the geomagnetic field, then the various phases of the wave may add destructively and fail to give rise to a significant polarization electric field. Dynamo fields generated within the different phases of the wave are shorted out by field-aligned currents in that case. Only if the wind has a stationary phase point can a net dynamo field be generated. A likely place for a stationary phase point to occur is near the magnetic dip equator where the projection of the neutral wind wave vector on the magnetic field line is small.

[16] So far, we have not commented on the effects of vertical winds. However, it is clear from both (5) and (7) (third term in numerator) that vertical winds affect vertical electric fields in the $E$ region in the same way as the zonal electric field. They therefore undergo the same amplification process in the electrojet and can, in principle, have a substantial impact on the electrojet current. *Anandarao et al.* [1978] report on 10–20 m/s vertical winds in the equatorial $E$ region measured with a twilight strontium release. *Raghavarao and Anandarao* [1980] argued that such a wind could reverse the direction of the electrojet current in some places and perhaps lead to counter electrojet conditions. However, the wind measurements of *Anandarao et al.* [1978] were made at a few heights only, and the calculations based on them employed considerable extrapolation. The role of vertical winds in contributing to the background state and day-to-day variability of the electrojet is not well established, thanks mainly to a shortage of pertinent data and reliable models. Certainly, vertical winds comparable to those measured recently by *Zhou* [2000] at Arecibo and by *Tao and Gardner* [1995] from Maui using contemporary experimental techniques would drastically affect the electrojet current if present at the dip equator and would represent an important local source of variability. The effects of vertical winds lay outside the scope of the analysis which follows, however, since we currently have no means of predicting, measuring, or inferring them.

[17] Finally, the fourth and last term in the numerator of (7) shows that a net vertical current flux arising in the electrojet at some altitude will necessitate the emergence of a vertical electric field at higher altitudes to maintain current continuity. In regions where the integrated Pedersen conductivity and, consequently, the denominator of (7) become small, the implied vertical electric field can become large. This situation occurs in the valley region above the electrojet and contributes to westward, countervailing plasma drifts there in the nighttime sector [*Haerendel and Eccles*, 1992]. The relative importance of the four terms in the numerator of (7) in setting up these countervailing drifts has not been clearly established.

## 3. Three-Dimensional Computational Model

[18] A quantitative treatment of low-latitude ionospheric electrodynamics requires consideration of the effects of finite parallel conductivity as well as the effects of spatial conductivity gradients in three dimensions. Here, we describe a three-dimensional steady-state potential model of an ionospheric plasma subject to prescribed forcing by winds and background electric fields. The model, which is similar to the one described by *Forbes and Lindzen* [1976], is based on the application of the quasineutrality condition to a realistic plasma in a dipole magnetic field and includes the effects of finite parallel conductivity. The quasineutrality condition can be expressed in polar coordinates as:

$$\nabla \cdot (\boldsymbol{\Sigma} \cdot \nabla \Phi) = \nabla \cdot (\boldsymbol{\Sigma} \cdot (\mathbf{E}_\circ + \mathbf{u} \times \mathbf{B})) \tag{8}$$

where $\boldsymbol{\Sigma}$ are the components of a second rank tensor conductivity expressed in polar coordinates. Expressions for these components were given by *Forbes* [1981] and are reproduced below in slightly modified form.

$$\begin{aligned}
\Sigma_{rr} &= \sigma_P \cos^2 I + \sigma_\circ \sin^2 I \\
\Sigma_{r\theta'} &= \Sigma_{\theta' r} = (\sigma_P - \sigma_\circ) \cos I \sin I \\
\Sigma_{r\phi} &= -\Sigma_{\phi r} = -\sigma_H \cos I \\
\Sigma_{\theta'\theta'} &= \sigma_P \sin^2 I + \sigma_\circ \cos^2 I \\
\Sigma_{\theta'\phi} &= -\Sigma_{\phi\theta'} = -\sigma_H \sin I \\
\Sigma_{\phi\phi} &= \sigma_P
\end{aligned}$$

where $I$ is the magnetic dip angle and $\theta'$ is the magnetic latitude.

[19] Equation (8) represents a non-separable linear inhomogeneous elliptic partial differential equation with non-constant coefficients and with cross-derivative terms for the electrostatic potential $\Phi(r, \theta', \phi)$ which can be discretized and solved numerically in three dimensions using conventional relaxation methods. Arbitrary forcing can be specified through the right side of (8). The coefficient matrices involved depend on the conductivities which, in turn, depend on the ionospheric plasma concentration and composition along with the collision frequencies, themselves dependent on neutral temperature, concentration, and composition. We have calculated the conductivities using ion-neutral and electron-neutral collision frequency expressions derived by *Richmond* [1972] and *Gagnepain et al.* [1977] and reproduced by *Forbes* [1981] in his equations 27–30. These apply to a three component plasma ($NO^+$, $O_2^+$, $O^+$) in a three component atmosphere ($N_2$, $O_2$, O) and include temperature corrections to account for short-range repulsion and resonant charge exchange effects. The electron-ion collision frequency is calculated according to the expression given by *Nicolet* [1953] and added to the electron-neutral collision frequency in the computation of the direct conductivity. Model atmospheric and ionospheric parameters are derived from the MSIS and IRI models, respectively [*Hedin et al.*, 1996; *Bilitza et al.*, 1993]. In evaluating the model con-

ductivities, we use a dipole magnetic field model but allow for a tilt between the geographic and geomagnetic meridians.

[20] Iterative techniques for solving discretized elliptic partial differential equations typically converge slowly and often prove impractical for addressing problems on large grids. For example, the gain factor for errors in a Jacobi or Gauss Siedel iteration method is given by $1 - \mathcal{O}(n^{-2})$, where $n$ is the number of grid points along a dimension of the simulation space [see, e.g., *Ames*, 1977]. Convergence is slow except when the grid is small. In effect, errors diminish as if undergoing diffusion, and only errors with scale sizes comparable to the grid size vanish rapidly. Slow convergence implies particularly high computational cost for three-dimensional problems.

[21] We have solved (8) computationally using a multigrid method like the one described by *Adams* [1991, 1989] and references therein. Multigrid methods improve upon iterative schemes by computing coarse grid approximations interleaved with fine grid refinements. Large-scale features converge rapidly in the coarse grid computations while fine structure is retained in the full grid computations. Approximate solutions and corrections are transmitted between multiple grid levels by interpolation and extrapolation operators. Reviews of multigrid algorithms have been presented by *Fulton et al.* [1986], *Press et al.* [1988], and *Hackbusch and Trottenberg* [1991].

[22] Our solution space is a section of the low-latitude ionosphere in the Peruvian sector centered on a point on the dip equator at 12.5°S, 77°W. The magnetic field declination is 0.6°. Altitudes between 80 and 150 km are included in the model, and the latitude and longitude extent is ±10°. Local time variations are included as variations in longitude. The number of grid points in $r$, $\theta'$, and $\phi$ are 73, 73, and 37, respectively. The boundary conditions imposed are that no current is allowed to flow through the lower boundary while no field-aligned current flows through the upper boundary. Additionally, Neumann boundary conditions are imposed on the perturbation potential at the $\phi$ and $\theta'$ boundaries. Plasma densities, temperatures, and composition are derived from the IRI model while neutral temperatures and densities required to estimate plasma collision frequencies are derived from MSIS. Neutral winds are supplied by the NCAR TIME-GCM. The background zonal electric field is a free parameter.

### 3.1. Model Results

[23] Model calculations have been performed for quiet-time conditions corresponding to local noon in mid January, 2001, for the equatorial $E$ region in the Peruvian sector. Results are shown in Figure 2. The background zonal electric field has been set to 0.375 mV/m (see below). The winds have been set to zero for this run, which represents a baseline for later comparison. Figure 2 presents one- and two-dimensional cuts through the three-dimensional solution space. Unless otherwise noted, the cuts pass through the center of the simulation space. The results show that the equipotentials depart from dipole magnetic field lines below about 95 km. This is to be expected, since the dominance of the direct conductivity that gives rise to highly field-aligned equipotential structures at higher altitudes starts to break down at about this altitude. The vertical polarization electric field that drives the electrojet Hall current maximizes just above 100 km altitude at a value of ~12 mV/m according to this model. The electrojet current mainly flows in a narrow strip of latitudes ~5° wide and also maximizes at an altitude just above 100 km. The peak current density is ~13 $\mu A/m^2$. Significant current density also flows in the meridional direction in this zone and is part of a system of counter-rotating current vortices existing just northward and southward of the dip equator.

### 3.2. Wind Effects

[24] Figure 3 shows the wind profiles that we will use as a basis for driving the electric potential model. These were predicted by the NCAR thermosphere/ionosphere/mesosphere electrodynamics general circulation model (TIME-GCM) [*Roble and Ridley*, 1994; *Roble*, 1995]. The model is an extension of the older TIEGCM [*Richmond et al.*, 1992] down to 30 km and thus includes the physics and chemistry of the upper stratosphere and mesosphere. Gravity wave effects may be included through various parameterizations such as Rayleigh friction or that developed by *Fritts and Lu* [1993]. The model can be coupled to the NCAR community climate model (CCM2) that extends from the ground to 30 km. At each time step, the two models pass information through an interactive flux coupler which conserves energy, mass, and momentum. Alternatively, it can use National Center for Environment Prediction (NCEP) gridded analyses of geopotential heights, atmospheric temperatures, and winds based on assimilation of data from aircraft, radiosonde, satellites, ships, buoys, etc. The former technique will be applied here.

[25] The TIME-GCM model self-consistently calculates electrodynamic interactions in the coupled thermosphere and ionosphere, providing predictions of electric potential, fields, and currents along with the ion and neutral densities, temperatures, and velocities. The vertical coordinate is log pressure with 29 levels spaced at two grid points per scale height; the altitudes extend roughly from 30 to 500 km with the top altitude depending on the level of solar activity. Latitude/longitude resolution is 5 by 5 degrees. Required inputs for the model are prescriptions of the solar and geomagnetic activity. The latter provides high-latitude energy and momentum sources which are parameterized in the model version used here by three inputs: cross-polar-cap potential, total hemispheric power, and the $B_y$ component of the interplanetary magnetic field. These values are used to select the appropriate convection pattern from the empirical model of *Heelis et al.* [1982] and the auroral particle precipitation pattern based on the model of *Fuller-Rowell and Evans* [1987].

[26] Lower thermospheric winds measured with chemical release experiments (see summary by *Larsen* [2002]) very often have amplitudes in excess of 150 m/s and exhibit strong, narrow jets at $E$ region altitudes. While the profiles shown in Figure 3 have amplitudes peaking at well over 100 m/s, those peaks occur at ~90 km and are both smaller and lower than those observed. However, the phasing of the TIME-GCM wind profiles appears to be similar to what is observed experimentally; the wavelengths are also similar if somewhat long. Lacking an explicit theoretical model of the large winds and the underlying pseudotides, our approach here is to use the TIME-GCM horizontal winds, multiplied by a factor of 1.5, to drive our potential model. This is an approximation intended to gauge the effects that $E$ region

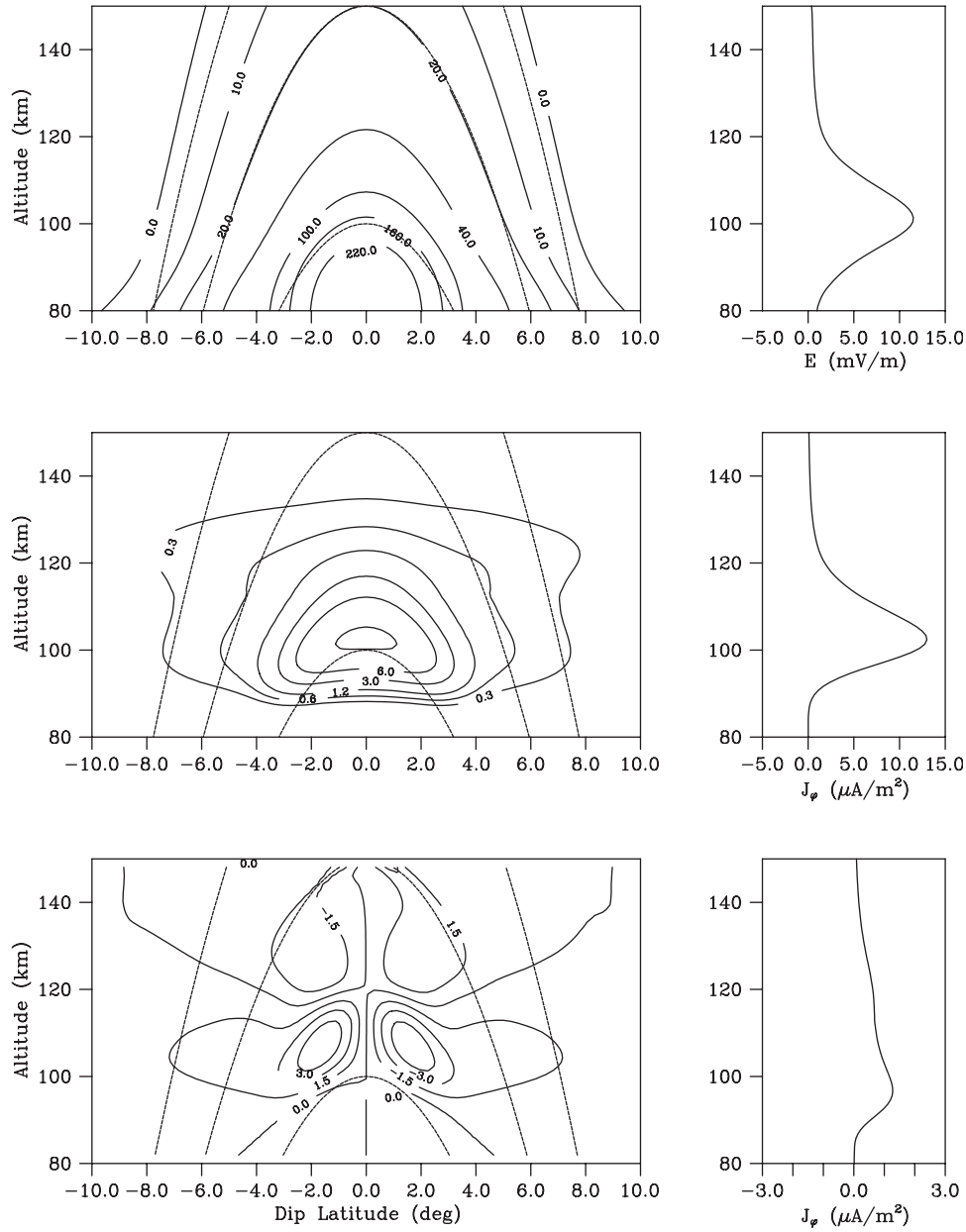


**Figure 2.** Results from numerical model of the equatorial electrojet current system. Dashed lines represent dipole magnetic field lines. (Top left) Electrostatic potential in Volts versus altitude in km and dip latitude in degrees. (Middle left) Zonal current density in $\mu$A/m$^2$. (Bottom left) Meridional current density. (Top right) Vertical polarization electric field profile at 0.5° dip latitude. (Middle right) Zonal current density profile at 0.5° dip latitude. (Bottom right) Zonal current density profile at 4° dip latitude.

winds comparable to those observed with chemical releases would have on the equatorial electrojet. The efficacy of this approximation will ultimately be borne out by radar observations which compare favorably with the potential model output. Note that the TIME-GCM lacks sufficient spatial resolution for studying the electrodynamics of the electrojet in detail. Furthermore, it treats magnetic field lines as equipotentials. We therefore use interpolated wind profiles produced by the TIME-GCM to force our potential model which exists on a much finer mesh grid. Note also that there have been no rocket measurements of lower thermospheric wind profiles in the daytime in the American sector that could be used to drive our model.

[27] Figure 4 shows model results for conditions identical to those used to produce Figure 2 except including neutral wind forcing. The winds used are those shown in the left panel of Figure 3 except that the zonal winds have been multiplied by a factor of 1.5. Changes to the current distribution brought about by the introduction of the winds are subtle close to the dip equator but grow more noticeable with increasing dip latitude. Near the dip equator, the main effect of the zonal wind is to modify the vertical polarization electric field. To a good approximation, this field has been increased by $|u_x B|$. This signifies that the *E* region neutral wind dynamo is operating very efficiently near the dip equator, where the magnetic flux tubes are nearly

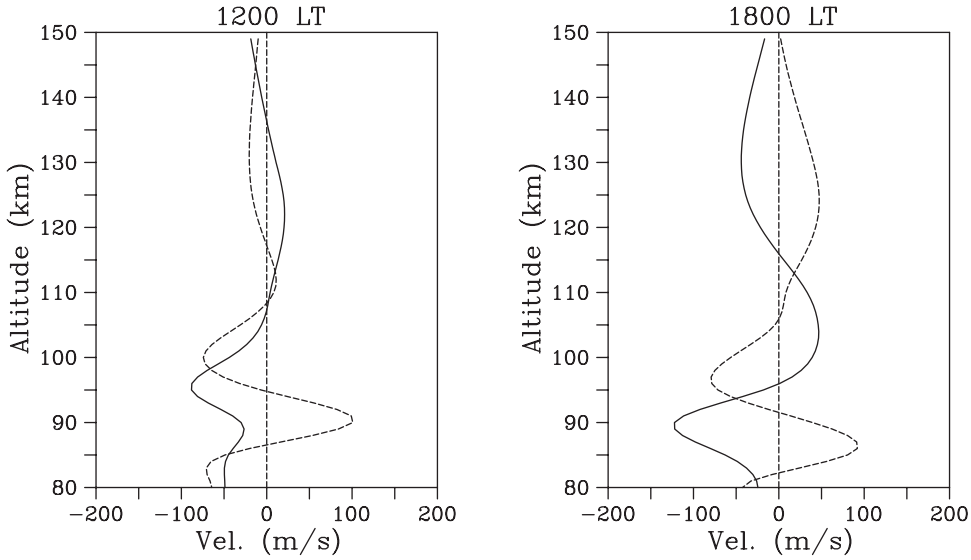


**Figure 3.** Neutral winds in the equatorial *E* region predicted by the NCAR TIME-GCM model for the Peruvian sector. Solid (dashed) lines represent zonal (meridional) winds.

horizontal at altitudes where the Pedersen conductivity is concentrated. Consequently, a significant portion of the total polarization electric field strength at the dip equator is wind driven.

[28] At higher dip latitudes, where magnetic field lines subtend different phases of the neutral wind field at altitudes where the Pedersen conductivity is concentrated, the dynamo is less efficient and less effective in negating wind driven current. Below about 120 km altitude, the response of the ions to the zonal neutral winds is mainly to move with them. The polarization electric field, meanwhile, is governed by the flux-tube-averaged zonal winds, and the $\mathbf{E} \times \mathbf{B}$ drifting electrons consequently lag the ions. A significant wind-driven zonal current results at high dip latitudes below about 120 km. The effect is sufficiently strong to reverse the direction of the *E* region zonal current density at dip latitudes greater than about 3°. The reversal of the zonal current is very evident in the central panel of Figure 4 which consequently looks quite different from the same panel in Figure 2 at high latitudes and at altitudes below about 120 km, particularly where the wind is strongest. This phenomenon has been modeled and described by *Anandarao and Raghavarao* [1979]. Above about 120 km where the ions are marginally magnetized, the main effect of the zonal winds is to drive significant meridional current in the $\mathbf{u} \times \mathbf{B}$ direction. The Pedersen current driven by the polarization electric field that opposes the $\mathbf{u} \times \mathbf{B}$ current cannot, once again, entirely negate it at these dip latitudes. Lastly, meridional winds can be seen in Figure 4 to drive discernible meridional currents at dip latitudes greater than about 5° at altitudes of 90 and 100 km where the wind amplitudes are greatest.

[29] Finally, Figure 5 shows model results for twilight conditions (1800 LT). The winds used for this run are the ones shown in the right panel of Figure 3, with the zonal component again multiplied by a factor of 1.5. The background zonal electric field was set to 0.425 mV/m for this run (see below). Similar remarks hold for this simulation as for the daytime case. Since the phasing of the horizontal winds has changed, however, so has the sense (sign) of the wind-induced current and electric field perturbations caused by the winds at different altitudes. Note that the magnitude of the current densities are greatly reduced in accordance with the reduced twilight number densities.

## 4. Ionospheric Irregularities as Tracers

[30] In the previous section, a static model of the equatorial electrojet showed how the vertical polarization electric field at the magnetic dip equator is directly influenced by the zonal wind driving the *E* region dynamo. Here, we present indirect evidence that the winds present in the lower thermosphere in the Peruvian sector are qualitatively similar to those assumed in the model calculations above. If we were concerned with another latitude regime, it would be possible to compare the polarization electric field and/or current density predictions in Figures 4 and 5 with direct, incoherent scatter radar-derived measurements. However, incoherent scatter techniques are generally inapplicable in the *E* region over Jicamarca because of the almost continuous presence of plasma irregularities in the electrojet and the resulting, intense coherent scatter and radar clutter. However, it is possible to make inferences about the electric field in the electrojet region on the basis of the coherent scatter from the irregularities.

### 4.1. Dispersion Relation

[31] A linear, local dispersion relation for the frequency $\omega$ and growth rate $\gamma$ of plasma irregularities which form in the equatorial electrojet has been derived by numerous researchers including *Fejer et al.* [1975] and may be expressed approximately as:

$$\omega = \frac{\mathbf{k} \cdot (\mathbf{V}_{de} - \mathbf{V}_{di})}{1 + \psi} + \mathbf{k} \cdot \mathbf{V}_{di} \tag{9}$$

$$\gamma = \frac{1}{1 + \psi}\left[\frac{\psi}{\nu_i}\left((\omega - \mathbf{k} \cdot \mathbf{V}_{di})^2 - k^2 C_s^2\right) + \frac{k_\perp \nu_i}{k^2 L \Omega_i}(\omega - \mathbf{k} \cdot \mathbf{V}_{di})\right] - 2\alpha n_\circ \tag{10}$$

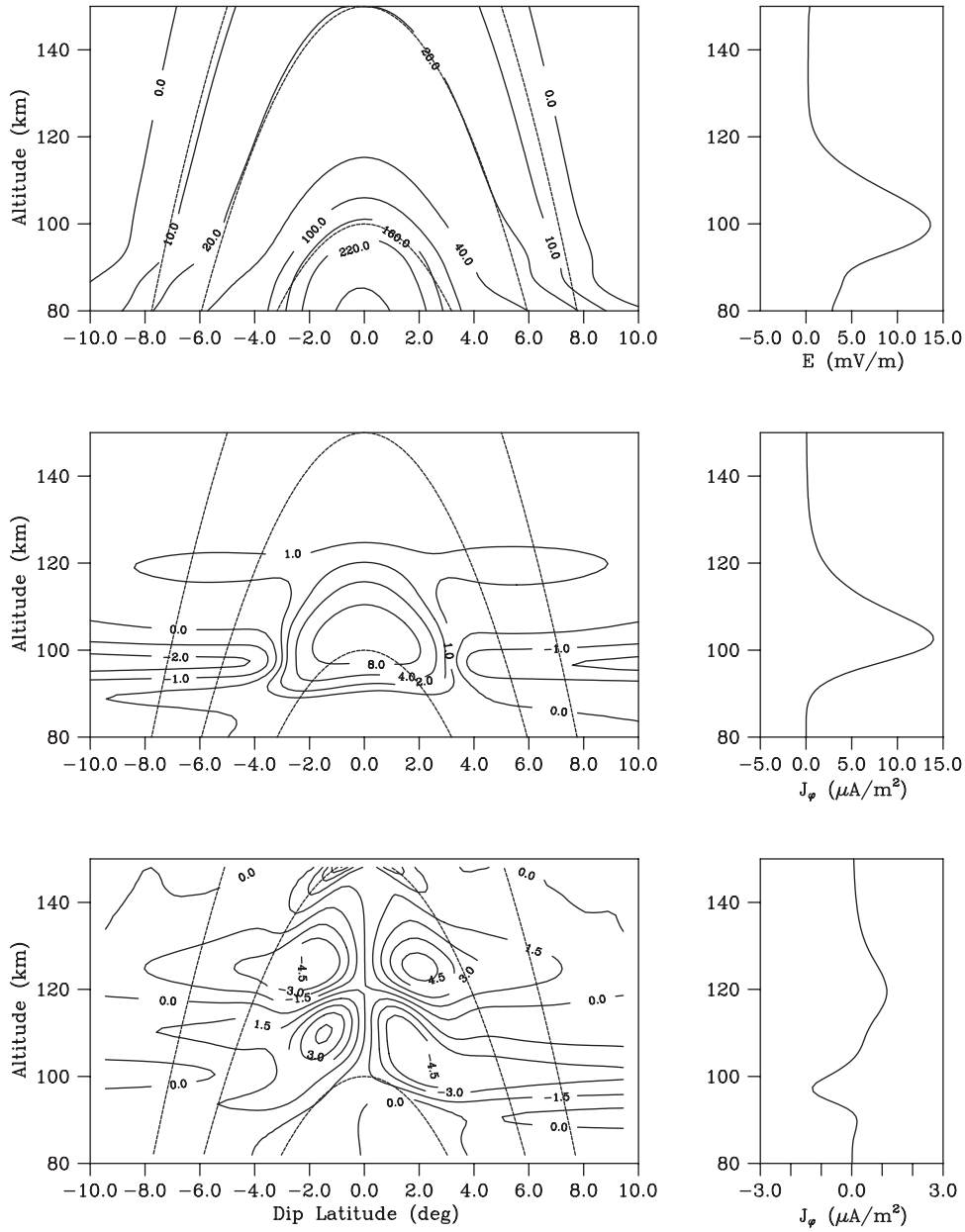


**Figure 4.** Same as Figure 2 except including wind forcing inspired by the daytime wind predictions shown in Figure 3. (Top left) Electrostatic potential in Volts versus altitude in km and dip latitude in degrees. (Middle left) Zonal current density in $\mu$A/m$^2$. (Bottom left) Meridional current density. (Top right) Vertical polarization electric field profile at 0.5° dip latitude. (Middle right) Zonal current density profile at 0.5° dip latitude. (Bottom right) Zonal current density profile at 4° dip latitude.

where $\psi$ is the anisotropy factor (the ratio of the electron to ion transverse mobility), $\nu_e$ and $\nu_i$ are the electron-neutral and ion-neutral collision frequencies, $\Omega_j$ refers to the gyrofrequency for species $j$, $C_s$ is the ion acoustic speed, $L$ is the vertical plasma density gradient scale length, and $\alpha$ is the recombination rate. Additionally, $k$ is the wavenumber, and $\mathbf{V}_{de}$ and $\mathbf{V}_{di}$ are the electron and ion drift velocities. Of the two terms in the square brackets in (10), the second is conventionally associated with gradient drift instabilities and the dispersion characteristics of the waves they generate. It is with such waves that we are mainly concerned here. We will use this dispersion relation to interpret radar scatter from small-scale irregularities in the equatorial electrojet and the so-called type II radar echoes that result (see *Farley* [1985] for review). Although these secondary waves are produced by nonlinear (three-wave) interactions between intermediate-scale primary gradient drift waves, experience has shown that (9) in particular appears to describe their propagation and that (10) is useful for indicating the conditions under which the ionosphere will become unstable [see, e.g., *Fejer and Kelley*, 1980]. Note that (10) implies that currents alone drive instabilities, and only where $\psi$ is not much larger than unity; winds alone generally do not destabilize the

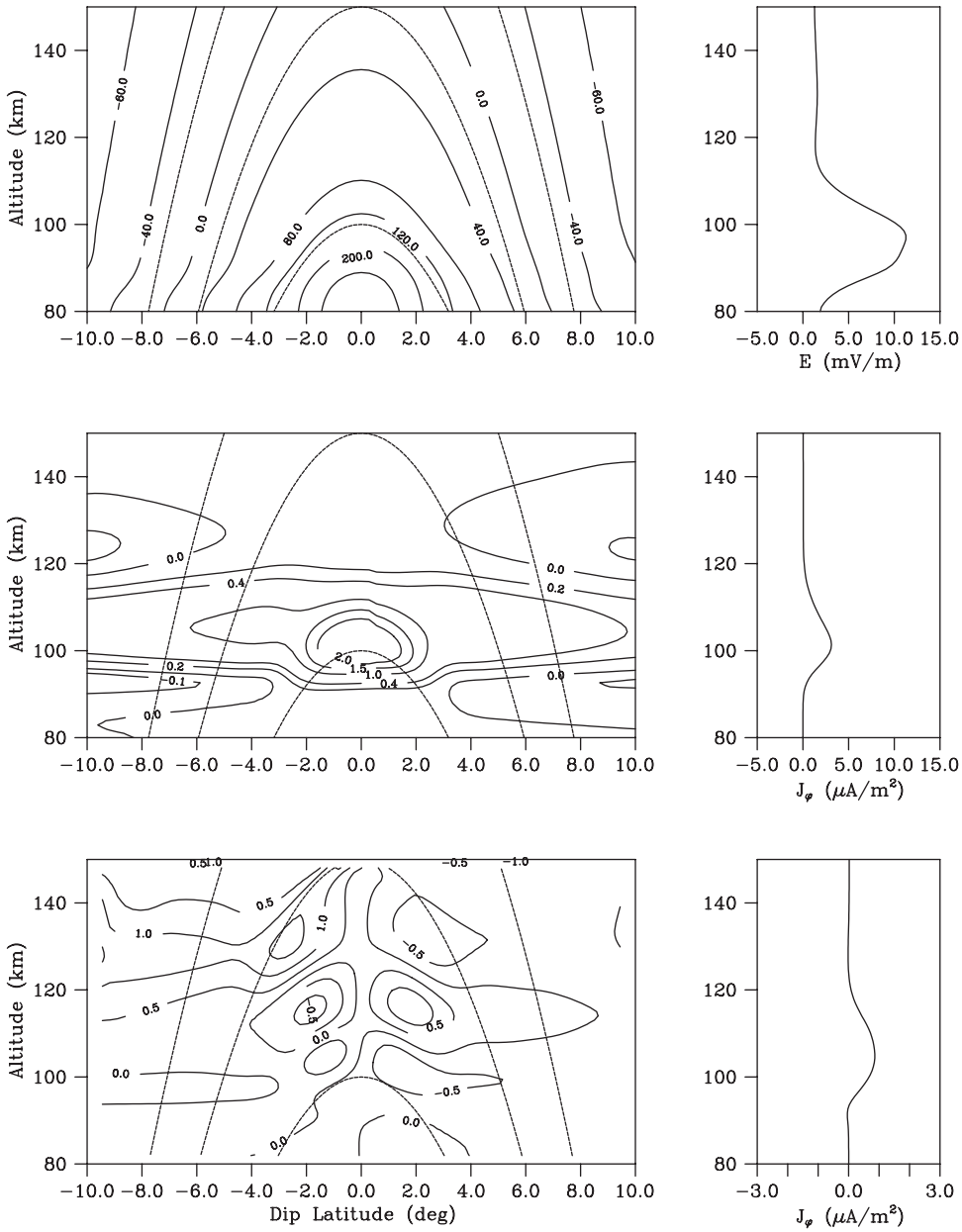


**Figure 5.** Same as Figure 4 except for twilight conditions. (Top left) Electrostatic potential in Volts versus altitude in km and dip latitude in degrees. (Middle left) Zonal current density in $\mu$A/m$^2$. (Bottom left) Meridional current density. (Top right) Vertical polarization electric field profile at 0.5° dip latitude. (Middle right) Zonal current density profile at 0.5° dip latitude. (Bottom right) Zonal current density profile at 4° dip latitude.

equatorial *E* region in zones where the dynamo can operate efficiently.

[32] Coherent radar echoes from type II electrojet plasma irregularities are observed at altitudes between about 95 and 105 during most of the daytime although, just prior to sunset, the layer from which backscatter is received rises and broadens markedly. In that altitude regime, the electrons are strongly magnetized. The ions are coupled strongly to the neutrals but have small Pedersen and $\mathbf{u} \times \mathbf{B}$ drift components in the electrojet at the upper limit of this altitude regime. Using (9), is a straightforward matter to predict the Doppler shift of type II echoes on the basis of the model winds and electric fields shown in the previous section. This is the basis for our model data comparisons.

### 4.2. Radar Observations

[33] A new antenna array has been installed at Jicamarca to make oblique observations of coherent backscatter from the electrojet. The main beam of the antenna, an array of 16 widely-spaced, tilted Yagi elements, is directed westward at a zenith angle of ~45° and has a half-power full beam width of ~1.9°. For the purposes of this paper, we regard the radiation pattern of the array as a pencil beam. The backscatter spectra observed with this array generally show

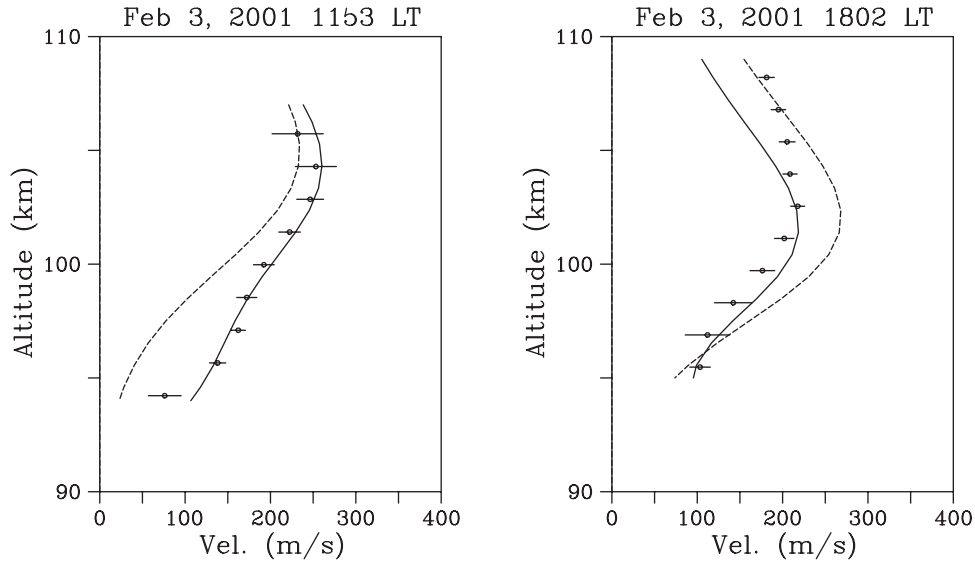


**Figure 6.** Plotter symbols with error bars represent Doppler shifts of oblique type II electrojet echoes measured at Jicamarca. Solid lines plotted through the symbols are Doppler shifts predicted on the basis of the model runs shown in Figures 4 and 5. Dashed lines represent equivalent model results except with wind forcing turned off. The panels at left and right represent noon and twilight conditions, respectively. Positive values imply westward wave propagation.

evidence of both type I and type II echoes. Our experimental procedure is to fit the spectra with a superposition of two Gaussian curves and to interpret the Doppler shift of the component with the greater width as the phase speed of the type II echo. The altitude where the echoes originate is computed from their range on the basis of the scattering geometry. We assume that the measured Doppler shifts are predicted by (9), which can be evaluated using results from our model runs.

[34] Figure 6 presents Doppler shifts of type II echoes measured using the oblique-looking antenna array at Jicamarca. Measurements for intervals near local noon and twilight are shown (plotter symbols) along with their statistical error bars. Positive values imply westward wave propagation. The integration time for the measurements was ~6 min. Also plotted are predictions for the measurements based on the model runs described above. Solid (dashed) lines represent runs with (without) neutral wind forcing. Note that the zonal electric field values used in those runs were chosen to optimize the agreement between the radar data and the wind-forced models and were not measured directly. These values (0.375 mV/m daytime, 0.425 mV/m twilight) are quite close to the seasonal average zonal electric fields predicted by *Scherliess and Fejer* [1999] and are also close to electric field estimates derived from backscatter data taken simultaneously using a broad-beam antenna and analyzed following the method of *Balsley* [1973] and *Hysell and Burcham* [2000].

[35] Clearly, the difference between the noontime radar data and the model predictions narrows dramatically with the inclusion of the TIME-GCM zonal winds. Note in particular that it would be impossible to account for the large (>100 m/s) Doppler shifts observed during the day below about 100 km (where the anisotropy factor $\psi$ is comparable or larger than unity) without incorporating strong, westward neutral winds at these altitudes. With the inclusion of the TIME-GCM predicted zonal winds, the agreement between the radar observations and the model prediction becomes remarkably close in this case. This is partly fortuitous, since Doppler profiles measured this way in the electrojet exhibit considerable qualitative day-to-day variability. The noontime profiles presented by *Tsunoda and Ecklund* [1999], for example, showed eastward wave propagation below about 96 km in contrast to the strong westward propagation evidenced here. Several days of radar observations were made at Jicamarca in January and February of 2001, however, and the shapes of the daytime profiles were generally similar to the one shown here. While the horizontal winds in the equatorial electrojet region may not mimic the TIME-GCM predictions faithfully every day, Figure 6 attests at least to the presence of strong winds in the equatorial lower thermosphere and the resulting effects on the electrojet plasma irregularities in the region.

[36] Turning to the results for 1800 LT, we see that the observed Doppler shift profile has a much less pronounced peak than the wind-free model profile would predict. At 1800 LT, the TIME-GCM zonal winds are eastward in the electrojet region and consequently have the effect, when incorporated in the model, of reducing the predicted westward phase speed of the plasma waves responsible for type II echoes. The nodes of the model zonal wind are at approximately 96 and 116 km at this time. The winds therefore do tend to flatten the predicted profile shape in the lower half of the electrojet region and would do so in the upper half if the upper node was lower, closer to 110 km. Indeed, the large amplitude waveforms in the nighttime neutral wind profiles presented by *Larsen and Odom* [1997] had vertical wavelengths close to 15 km at E region altitudes rather than the ~20–30 km wavelengths evident in Figure 3. We hypothesize that the actual zonal winds in the lower thermosphere had the appropriate wavelength and phasing to offset the background zonal phase speeds of the

plasma irregularities and, thereby, to flatten the profiles shown in Figure 6. If this phenomenon occurs repeatedly, it would help to explain the very flat electrojet phase speed profiles often observed at twilight with radar interferometry [*Hysell and Burcham*, 2000].

[37] Note once more that phase speed profiles measured on other occasions in the electrojet over Jicamarca at twilight reveal considerable day-to-day variability, and we should not expect to reproduce exactly any given data set with runs from a model that does not include the factors that control this variability. However, Figure 6 shows at once that neutral wind effects are required to explain the spectra of coherent scatter from the electrojet and that the winds predicted by the NCAR TIME-GCM model seem to have roughly the correct wavelength and phasing to help account for the radar observations.

## 5. Conclusion

[38] The increasing emphasis on the importance of nontidal wind motions in the equatorial lower thermosphere and the realization that wind speeds in excess of 150 m/s are commonplace in the *E* region invite an examination of the consequences for the equatorial electrojet and for ionospheric electrodynamics in general. We have reviewed the fundamental principles that relate neutral winds and electric fields in the *E* region ionosphere at low latitudes and applied these principles to interpreting representative, test case radar observations made in the electrojet over Jicamarca. The observations strongly suggest that large horizontal neutral winds, of the order of up to 150 m/s, are required to account for the Doppler shifts of type II echoes originating in the electrojet. Wind profiles generated by the NCAR TIME-GCM model can bring about reasonable model-data agreement, particularly during the day, but only if the amplitudes of the model zonal winds are increased by about 50% in the *E* region. Better agreement still would result if the NCAR model could reproduce the wind features with $\sim$15 km vertical wavelengths seen in chemical release experiments at *E* region altitudes. This may necessitate improving the vertical resolution of the NCAR model or modifying the specification of the lower boundary conditions.

[39] Further improvement in model-data agreement is not anticipated until the sources of day-to-day variability in the lower thermospheric wind structure and electrojet current system are better understood and incorporated into the various models. Routine neutral wind measurements, at night and particularly during the day, are required to advance this research, as is a means of directly measuring electric fields and plasma densities in the equatorial *E* region.

[40] **Acknowledgments.** This work was supported by the National Science Foundation through cooperative agreement ATM-9911209 to Cornell University, by NSF grant ATM-0080338 to Clemson University, and by NSF grant ATM-9813863 to the University of Texas at Dallas. The Jicamarca Radio Observatory is operated by the Geophysical Institute of Peru, Ministry of Education, with support from the NSF cooperative agreements just mentioned. The help of the staff was much appreciated. We are indebted also to R. Roble for providing us with runs of the NCAR TIME-GCM model and to M. F. Larsen for his helpful comments. We also thank NCAR's Scientific Computing Division for providing computing time. The MUDPACK package used for this research (copyright John C. Adams) was obtained from the University Corporation for Atmospheric Research, which is sponsored by the National Science Foundation.

[41] Janet G. Luhmann thanks Graham J. Bailey and Alan Burns for their assistance in evaluating this paper.

## References

Adams, J., MUDPACK: Multigrid FORTRAN software for the efficient solution of linear elliptic partial differential equations, *Appl. Math. Comput.*, *34*, 113, 1989.

Adams, J., Multigrid software for elliptic partial differential equations: MUDPACK, *Tech. Note 357+STR*, Natl. Cent. for Atmos. Res., Boulder, Colo., 1991.

Ames, W. F., *Numerical Methods for Partial Differential Equations*, Academic, San Diego, Calif., 1977.

Anandarao, B. G., and R. Raghavarao, Effects of vertical shears in the zonal winds on the electrojet, *Space Res.*, *XIX*, 283, 1979.

Anandarao, B. G., R. Raghavarao, and C. R. Reddi, Electric fields by gravity wave winds in the equatorial ionosphere, *J. Geophys. Res.*, *82*, 1510, 1977.

Anandarao, B. G., R. Raghavarao, J. N. Desai, and G. Haerendel, Vertical winds and turbulence over Thumba, *J. Atmos. Terr. Phys.*, *40*, 157, 1978.

Balsley, B. B., Electric fields in the equatorial ionosphere: A review of techniques and measurements, *J. Atmos. Terr. Phys.*, *35*, 1035, 1973.

Balsley, B. B., B. G. Fejer, and D. T. Farley, Radar measurements of neutral winds and temperatures in the equatorial *E* region, *J. Geophys. Res.*, *81*, 1457, 1976.

Bilitza, D., K. Rawer, L. Bossy, and T. Gulyaeva, International Reference Ionosphere: Past, present, future, *Adv. Space Res.*, *13*(3), 3, 1993.

Chau, J. L., D. T. Farley, and B. B. Balsley, East-west asymmetry in type 1 electrojet echoes at Jicamarca, paper presented at X International Symposium on Equatorial Aeronomy, U.S. Natl. Sci. Found., Antalya, Turkey, 17–23 May 2000.

Crain, D. J., R. A. Heelis, and G. J. Bailey, Effects of electrical coupling on equatorial ionospheric plasma motions: When is the *F* region a dominant driver in the low-latitude dynamo?, *J. Geophys. Res.*, *98*, 6033, 1993.

Devasia, C. V., and C. A. Reddy, Retrieval of east-west wind in the equatorial electrojet from the local wind generated electric field, *J. Atmos. Terr. Phys.*, *57*, 1233, 1995.

Du, J., and R. J. Stening, Simulating the ionospheric dynamo, II, Equatorial electric fields, *J. Atmos. Sol. Terr. Phys.*, *61*, 925, 1999.

Fambitakoye, O., P. N. Mayaud, and A. D. Richmond, Equatorial electrojet and regular daily variation $S_R$ III, Comparison of observations with a physical model, *J. Atmos. Terr. Phys.*, *38*, 113, 1976.

Farley, D. T., A theory of electrostatic fields in a horizontally stratified ionosphere subject to a vertical magnetic field, *J. Geophys. Res.*, *64*, 1225, 1959.

Farley, D. T., A theory of electrostatic fields in the ionosphere at nonpolar geomagnetic latitudes, *J. Geophys. Res.*, *65*, 869, 1960.

Farley, D. T., Theory of equatorial electrojet plasma waves: New developments and current status, *J. Atmos. Terr. Phys.*, *47*, 729, 1985.

Farley, D. T., E. Bonelli, B. G. Fejer, and M. F. Larsen, The prereversal enhancement of the zonal electric field in the equatorial ionosphere, *J. Geophys. Res.*, *91*, 13,723, 1986.

Fejer, B. G., The equatorial ionospheric electric fields: A review, *J. Atmos. Terr. Phys.*, *43*, 377, 1981.

Fejer, B. G., and M. C. Kelley, Ionospheric irregularities, *Rev. Geophys*, *18*, 401, 1980.

Fejer, B. G., D. T. Farley, B. B. Balsley, and R. F. Woodman, Vertical structure of the VHF backscattering region in the equatorial electrojet and the gradient drift instability, *J. Geophys. Res.*, *80*, 1313, 1975.

Forbes, J. M., The equatorial electrojet, *Rev. Geophys.*, *19*, 469, 1981.

Forbes, J. M., and R. S. Lindzen, Atmospheric solar tides and their electrodynamic effects, II, The equatorial electrojet, *J. Atmos. Terr. Phys.*, *38*, 911–920, 1976.

Fritts, D. C., and W. Lu, Spectral estimates of gravity wave energy and momentum fluxes, II, Parameterization of wave forcing and variability, *J. Atmos. Sci.*, *50*, 3695, 1993.

Fuller-Rowell, T. J., and D. S. Evans, Height-integrated Pedersen and Hall conductivity patterns inferred from the TIROS-NOAA satellite data, *J. Geophys. Res.*, *92*, 7606, 1987.

Fulton, S., R. Ciesielski, and W. Schubert, Multigrid methods for elliptic problems: A review, *Mon. Weather Rev.*, *114*, 943, 1986.

Gagnepain, J., M. Crochet, and A. D. Richmond, Comparison of equatorial electrojet models, *J. Atmos. Terr. Phys.*, *39*, 1119, 1977.

Hackbusch, W., and U. Trottenberg, *Multigrid Methods III*, Birkhäuser Boston, Cambridge, Mass., 1991.

Haerendel, G., and J. V. Eccles, The role of the equatorial electrojet in the evening ionosphere, *J. Geophys. Res.*, *97*, 1181, 1992.

Haerendel, G., J. V. Eccles, and S. Cakir, Theory for modeling the equatorial evening ionosphere and the origin of the shear in the horizontal plasma flow, *J. Geophys. Res.*, *97*, 1209, 1992.

Hedin, A. E., et al., Empirical wind model for the upper, middle, and lower atmosphere, *J. Atmos. Terr. Phys.*, *58*, 1421, 1996.

Heelis, R. A., P. C. Kendall, R. J. Moffet, D. Windle, and H. Rishbeth, Electric coupling of the *E* and *F* regions and its effect of the *F* region drifts and winds, *Planet. Space Sci.*, *22*, 743, 1974.

Heelis, R. A., J. K. Lowell, and R. W. Spiro, A model of the high-latitude ionospheric convection pattern, *J. Geophys. Res.*, *87*, 6339, 1982.

Hysell, D. L., and J. Burcham, Ionospheric electric field estimates from radar observations of the equatorial electrojet, *J. Geophys. Res.*, *105*, 2443, 2000.

Kato, S., Electric field and wind motion at the magnetic equator, *J. Geophys. Res.*, *78*, 757, 1973.

Kudeki, E., and S. Bhattacharyya, Postsunset vortex in equatorial *F* region plasma drifts and implications for bottomside spread- *F*, *J. Geophys. Res.*, *104*, 28,163, 1999.

Kudeki, E., B. G. Fejer, D. T. Farley, and H. M. Ierkic, Interferometer studies of equatorial *F* region irregularities and drifts, *Geophys. Res. Lett.*, *8*, 377, 1981.

Kudeki, E., B. G. Fejer, D. T. Farley, and C. Hanuise, The Condor equatorial electrojet campaign: Radar results, *J. Geophys. Res.*, *92*, 13,561, 1987.

Larsen, M. F., Winds and shears in the mesosphere and lower thermosphere: Results from four decades of chemical release wind measurements, *J. Geophys. Res.*, *107*, 10.1029/2001JA000218, in press, 2002.

Larsen, M. F., and C. D. Odom, Observations of altitudinal and latitudinal *E*-region neutral wind gradients near sunset at the magnetic equator, *Geophys. Res. Lett.*, *24*, 1711, 1997.

Larsen, M. F., and R. L. Walterscheid, Modified geostrophy in the thermosphere, *J. Geophys. Res.*, *100*, 17,321, 1995.

Nicolet, M., The collision frequency of electrons in the ionosphere, *J. Atmos. Terr. Phys.*, *3*, 200, 1953.

Press, W. H., B. P. Flannery, S. A. Teukolsky, and W. T. Vetterling, *Numerical Recipes in C*, Cambridge Univ. Press, New York, 1988.

Raghavarao, R., and B. G. Anandarao, Vertical winds as a plausible cause for equatorial counter electrojet, *Geophys. Res. Lett.*, *7*, 357, 1980.

Reddy, C. A., and C. V. Devasia, Equivalent circuit analysis of neutral wind effects on equatorial electrojet, *Nature*, *273*, 195, 1978.

Reddy, C. A., and C. V. Devasia, Height and latitude structure of electric fields and currents due to local east-west winds in the equatorial electrojet, *J. Geophys. Res.*, *86*, 5751, 1981.

Reddy, C. A., B. T. Vikramkumar, and K. S. Viswanathan, Electric fields and currents in the equatorial electrojet deduced from VHF radar observations, I, A method of estimating electric fields, *J. Atmos. Terr. Phys.*, *49*, 183, 1987.

Richmond, A. D., Numerical model of the equatorial electrojet, *Tech. Rep. AFCRL-72-0668, ERP 421*, Air Force Cambridge Res. Lab., Hanscom AFB, Bedford, Mass., 1972.

Richmond, A. D., Equatorial electrojet, I, Development of a model including winds and instabilities, *J. Atmos. Terr. Phys.*, *35*, 1083, 1973.

Richmond, A. D., E. C. Ridley, and R. G. Roble, A thermosphere/ionosphere general circulation model with coupled electrodynamics, *Geophys. Res. Lett.*, *19*, 601, 1992.

Rishbeth, H., Polarization fields produced by winds in the equatorial *F* region, *Planet. Space Sci.*, *19*, 357, 1971.

Rishbeth, H., The *F* region dynamo, *J. Atmos. Terr. Phys.*, *43*, 387, 1981.

Roble, R. G., Energetics of the mesosphere and thermosphere, in *The Upper Mesosphere and Lower Thermosphere, Geophys. Monogr. Ser.*, vol. 87, p. 1, AGU, Washington, D. C., 1995.

Roble, R. G., and E. C. Ridley, A thermosphere-ionosphere-mesosphere-electrodynamics general circulation model (time-GCM): Equinox solar cycle minimum simulations (30–500 km), *Geophys. Res. Lett.*, *21*, 417, 1994.

Scherliess, L., and B. G. Fejer, Radar and satellite global equatorial *F* region vertical drift model, *J. Geophys. Res.*, *104*, 6829, 1999.

Tao, X., and C. S. Gardner, Heat flux observations in the mesopause region above Haleakala, *Geophys. Res. Lett.*, *22*, 2829, 1995.

Tsunoda, R. T., and W. L. Ecklund, On the nature of radar echoes below 95 km during counter streaming in the equatorial electrojet, *Geophys. Res. Lett.*, *26*, 2717, 1999.

Wharton, L. E., N. W. Spencer, and H. G. Mayr, The Earth's thermospheric superrotation from Dynamics Explorer 2, *Geophys. Res. Lett.*, *11*, 531, 1984.

Zhou, Q. H., Incoherent scatter radar measurements of vertical winds in the mesosphere, *Geophys. Res. Lett.*, *27*, 1803, 2000.

---

J. L. Chau, Radio Observatorio de Jicamarca, Instituto Geofísico del Perú, Apartado 13-0207, Lima 13, Peru. (chau@geo.igp.gob.pe)

C. G. Fesen, W. B. Hanson Center for Space Sciences, University of Texas at Dallas, MS FO22, P. O. Box 830688, Richardson, TX 75083-0688, USA. (fesen@tides.utdallas.edu)

D. L. Hysell, Earth and Atmospheric Sciences, Cornell University, 2108 Snee Hall, Ithaca, NY 14853, USA. (daveh@geology.cornell.edu)